9-3-2020

Direct P-wave anisotropy measurements at Homestake Mine: implications for wave propagation in continental crust

James Atterholt
Department of Earth and Atmospheric Sciences, Indiana University, Bloomington, IN

Sarah J. Brownlee
Department of Environmental Science and Geology, Wayne State University, Detroit, MI, sarah.brownlee@wayne.edu

Gary L. Pavlis
Department of Earth and Atmospheric Sciences, Indiana University, Bloomington, IN

Recommended Citation

Atterholt, J., Brownlee, S. J., Pavlis, G. L. (2020) Direct P-wave anisotropy measurements at Homestake Mine: implications for wave propagation in continental crust. Geophysical Journal International 224(1), 121-137. https://doi.org/10.1093/gji/ggaa416

Geophysical Journal International

Geophys. J. Int. (2020) **224,** 121–137
Advance Access publication 2020 September 03
GJI Seismology

doi: 10.1093/gji/ggaa416

Direct *P*-wave anisotropy measurements at Homestake Mine: implications for wave propagation in continental crust

James Atterholt,[1,*] Sarah J. Brownlee[2] and Gary L. Pavlis[1]

[1] *Department of Earth and Atmospheric Sciences, Indiana University,* 1001 *East* 10*th St., Bloomington, IN* 47405*, USA. E-mail: pavlis@indiana.edu*
[2] *Department of Geology, Wayne State University,* 0224 *Old Main, Detroit, MI* 48202*, USA*

Accepted 2020 August 14. Received 2020 July 22; in original form 2019 November 17

SUMMARY

We measured anisotropic seismic properties of schists of the Homestake Formation located at a depth of 1478 m in the Sanford Underground Research Facility (SURF) in the Black Hills of South Dakota, USA. We deployed a 24-element linear array of three-component geophones in an area in the Homestake Mine called 19-ledge. An airless jackhammer source was used to shoot two profiles: (1) a walkaway survey to appraise any distance dependence and (2) a fan shot profile to measure variations with azimuth. Slowness estimates from the fan shot profile show a statistically significant deviation with azimuth with the expected 180° variation with azimuth. We measured *P*-wave particle motion deviations from data rotated to ray coordinates using three methods: (1) a conventional principal component method, (2) a novel grid search method that maximized longitudinal motion over a range of search angles and (3) the multiwavelet method. The multiwavelet results were computed in two frequency bands of 200–600 and 100–300 Hz. Results were binned by azimuth and averaged with a robust estimation method with error bars estimated by a bootstrap method. The particle motion results show large, statistically significant variations with azimuth with a 180° cyclicity. We modelled the azimuthal variations in compressional wave speed and angular deviation from purely longitudinal particle motion of *P*-waves using an elastic tensor method to appraise the relative importance of crystalline fabric relative to fracturing parallel to foliation. The model used bulk averages of crystal fabric measured for an analogous schist sample from southeast Vermont rotated to the Homestake Formation foliation directions supplied by SURF from old mine records. We found with average crustal crack densities crack induced anisotropy had only a small effect on the observables. We found strong agreement in the traveltime data. The observed amplitudes of deviations of *P* particle motion showed significantly larger variation than the model predictions and a 20° phase shift in azimuth. We attribute the inadequacies of the model fit to the particle motion data to inadequacies in the analogue rock and/or near receiver distortions from smaller scale heterogeneity. We discuss the surprising variability of signals recorded in this experimental data. We show clear examples of unexplained resonances and unexpected variations on a scale much smaller than a wavelength that has broad implications for wave propagation in real rocks.

Key words: North America; Wavelet transform; Seismic anisotropy; Wave propagation; Wave scattering and diffraction.

1 INTRODUCTION

It is well known that metamorphic rocks dominate Earth's crust. A large fraction of metamorphic rocks have a 'fabric' defined by the preferred orientation of minerals. Numerous theoretical (e.g. Almqvist & Mainprice 2017) and experimental (e.g. Fouch & Rondenay 2006) results demonstrate that rocks with a metamorphic fabric have anisotropic elastic properties. Numerous studies also demonstrate that fractures induce anisotropic properties in upper crustal rocks (e.g. Liu & Crampin 1987; Crampin & Chastin 2003; Tsvankin et al 2010; Crampin & Gao 2013). Consequently, seismic waves propagating through the crust should be modelled as an

* Now at: Division of Geological and Planetary Sciences, California Institute of Technology, 1200 E California Blvd, Pasadena, CA 91125, USA

anisotropic medium. Until fairly recently, however, nearly all studies in seismology modelling wave propagation used models that assumed layered, isotropic media due to limitations in computing power. However, recent computational advances have made modelling 2-D and 3-D isotropic and anisotropic media feasible (e.g. Petersson & Sjorgreen 2015, 2017a,b). Furthermore, recent work by Okaya *et al.* (2019) provide a theoretical framework for constructing equivalent media approximations to field scale geologic structures like folding. Consequently, the isotropic, layered media assumption is no longer required to make progress on modelling seismic waveforms and a more solid understanding of how rock fabric affects wave propagation in the Earth is important.

A large body of literature in geologic mapping, petrology and mineral physics show that Earth is a heterogeneous, anisotropic medium due to preferred orientation of minerals and the rich, 3-D geometry of geologic structures. Further, as a medium created by mixing of material by the whole range of geologic processes that shaped the evolution of the Earth, the heterogeneity is almost certainly present at any scale we can observe it. All models we use for imaging the Earth are thus approximations. We assert a fundamental problem in seismology is the need to better understand how the reality of heterogeneous, anisotropic structure impacts measurable observables. An important contribution of this paper is new insight on how mineralogical to outcrop scale heterogeneity affect two observables: velocity variations with direction and *P*-wave particle motion deviations from longitudinal.

There are currently well-developed theories to predict anisotropic properties of rocks from textural data and mineral assemblages (Mainprice *et al.* 2015). Elastic properties of minerals have been measured by a range of techniques for decades and are available in standard compilations like those of Bass (1995) and Isaak (2001). There is also a large literature on direct measurements of wave speeds of rocks at hand sample scales (e.g. Christensen 1965, 1966; Christensen & Okaya 2007). The data set used in this study is unique in that it extends the scale of measurement to larger than hand samples (1–100 m), but one to two orders of magnitude smaller than the resolution achieved with crustal scale inversions. That is, the entire experiment was conducted in a single metamorphic rock formation (schist of the Homestake Formation) so an assumption of a homogenous, but anisotropic medium is not absurd. This allows us to measure anisotropic rock properties without the ambiguity of a structural inversion that characterizes most previous work (see e.g. reviews by Fouch & Rondenay 2006 and Romanowicz & Wenk 2017). In addition, the experiment depth (1.5 km) of this study eliminates the complexities of the weathered layer that influence all surface measurements. The depth also reduces, but does not eliminate the impact of fracture-induced anisotropy. A perspective on the scale to which these experimental data are relevant is that we are measuring anisotropic properties at scales smaller than the grid size for most 3-D finite difference simulation used in seismology. The results are also relevant to methods recently described by Okaya *et al.* (2019), which can be used to quantitatively predict how heterogeneity like folds map to seismic observables.

The focus of this paper is the analysis of a set of active source seismic experiments conducted in the Homestake Mine located in the Black Hills of South Dakota. Homestake was the deepest underground mine in North America before it shut down in the late 1990s. It is now home to an extensive underground research facility called the Sanford Underground Research Facility (SURF; https://sanfordlab.org/). SURF has hosted a range of experiments in many areas of science. The experiment analysed here was done in support of a complementary broad-band array experiment described by Mandic *et al.* (2018). We further focus this paper on the experiment we conducted at what Homestake geologists called 19-ledge on the 4850 level (a designation from the original mine for depth in feet from a local datum).

The anisotropy literature for body wave propagation is dominated by three techniques: shear wave splitting, methods based on *P* to *S* conversions from interfaces using the concept of *P* receiver functions (e.g. Fouch & Rondenay 2006; Schulte-Pelkam & Mahan 2014; Liu *et al.* 2015; Park & Levin 2016) and measurements of wave speed variations with direction. Complexities in the experimental data described below and the Supporting Information made *S*-wave splitting measurements challenging. The receiver function methods are not applicable for multiple reasons. We thus elected to focus exclusively on *P*-wave anisotropy measured by two fundamentally different approaches: velocity variations with azimuth and *P*-wave particle motion deviations from the longitudinal direction. The method of using velocity variations with azimuth to detect anisotropy has a long history. Traveltime analysis of oceanic refraction data by Hess (1964), in fact, provided the first clear evidence for anisotropic wave propagation in the Earth. Velocity variation with azimuth methods dominate seismology because the measurements are generally robust and repeatable (e.g. Shearer & Orcutt 1986; VanderBeek & Toomey 2017; Mark *et al.* 2019). This study is no exception, and we find clear evidence the rocks at Homestake are anisotropic from the analysis of traveltimes.

Particle motion measurements have a much more checkered history. Evidence of the truth of this statement can be gleaned from any electronic geoscience database. For example, one database we searched yielded 990 hits for 'shear wave splitting' but only 9 with '*P*-wave' and 'particle motion' in the publication title. We suspect this difference is caused by the fact that negative results are difficult to publish. Our experience is that particle motion measurements are subject to a lot of pitfalls that may explain this discrepancy. We thus assert an important additional contribution of this paper is that these data provide some hints on why *P*-wave particle motion estimates are so unreliable. We suggest the root of the problem is a fundamental, unresolved theoretical issue in how we model particle motion measurements quantitatively compared to reality: Earth is heterogeneous at all scales, but we normally approximate it as locally homogenous.

2 DATA

The experimental data analysed in this paper are a subset of data from a collaborative effort to appraise the feasibility of deploying an advanced LIGO (Laser Interferometer Gravitational-wave Observatory) system underground at SURF (Mandic *et al.* 2018). A summary of the overall experimental program is found in that paper. Here we only show results from what we called a horizontal seismic profile (HSP) experiment conducted on the 4850 level of the Homestake Mine (Fig. 1). We use the acronym HSP to emphasize the analogy to the experimental technique called the vertical seismic profile (VSP) developed by the petroleum industry (e.g. Hardage 1991). The experiment is effectively a VSP with the sensor array horizontal. The HSP used a fixed array of 24 three-component geophones spaced at 4-m intervals. The sensors were carefully oriented with a novel jig (see the Supporting Information) and fastened to the floor of the drift by one of two methods. Most sensors in this array were anchored with plaster of Paris to a concrete floor that

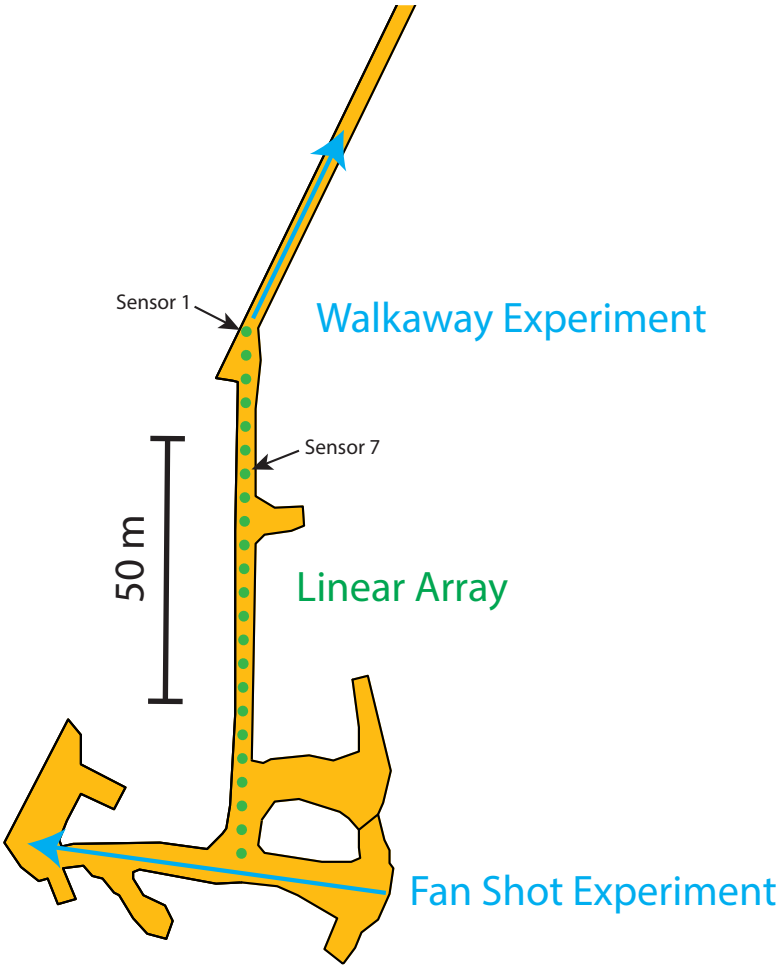

Figure 1. Schematic diagram of the experiment site. Yellow area is mine void (drifts) in which the experiment was conducted that were accessible. See the Supporting Information for the location of this site in relation to the rest of Homestake Mine and nearby drifts we could not enter. Drift geometry was provided by SURF. Green dots indicate the location of the seismometers at 4-m spacing. Blue arrows indicate the shooting direction of active source points. Walkaway experiment sources were spaced at 1-m intervals and fan shot experiment sources were spaced at 2-m intervals. Sensor 1 is at the north end of the line as illustrated and 24 is at the south end of the line. Sensor 7 is highlighted for reasons given in Section 6.

spanned the experimental area south of sensor 4. Those on the north end were anchored with plaster of Paris to the walls of the drift. For the HSP, we conducted two seismic experiments along a drift at the 4850 level of the mine: a fan-shot experiment in the drift nearly perpendicular to the array and a walkaway experiment conducted along the drift oblique to the array.

For the fan-shot experiment, we deployed a vertical, hammer force at 2-m intervals approximately perpendicular to the sensor array with the source passing within a few cm of the southernmost sensor (number 24). The walkaway experiment used both a vertical and transverse oriented (perpendicular to the drift direction) source fired at 1-m intervals on a profile at a small oblique angle to the array (Fig. 1). We show results here only from the vertical source data because the signal-to-noise ratio is much better than the transverse data. These walkaway and fan shot profiles complement each other. The fan-shot experiment yielded large azimuth variations, and the walkaway experiment yielded large distance variations with small azimuth variation. We collected two similar experiments on the 4100 level of the mine (see the Supporting Information), but we focus on the 4850 experiments because it was the only site in which we conducted a fan shot profile.

Fig. 2 shows a typical shot gather from the walkaway profile. The example illustrates three noteworthy things about these data. First, the signal-to-noise ratio is very good for all sensors. We found the maximum offset that yielded reasonable signals with this source was around 150 m, so we terminated the walkaway experiment when the source-to-receiver offset for the nearest sensor exceeded 40 m. Secondly, these data are extremely high frequency relative to comparable data collected with a surface array. As Fig. 3 shows, these data have significant signal up to 1 kHz for the entire range of source–receiver offsets. The peak source frequency is around 500 Hz, which is more than an order of magnitude higher than what we'd expect from a comparable experiment conducted at the surface. The reason for this difference is likely that a hammer source striking hard rock creates a sharper source pulse than a hammer source striking soil. Thirdly, a careful inspection of Fig. 2 shows a remarkably large waveform variation between adjacent sensors. We explore this issue at length in Section 6, but in relation to data quality, this waveform variation does not significantly impact picking first arrival times. The variation, however, undoubtedly creates significant scatter in particle motion measurements.

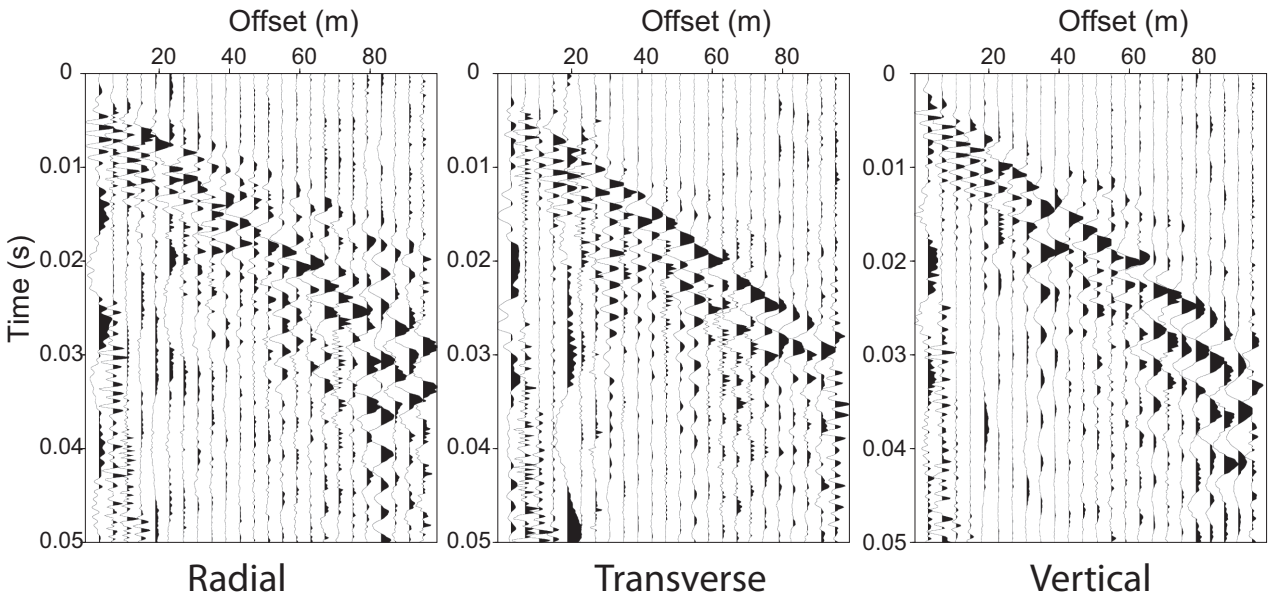

Figure 2. Example shot gathers. Example is one shot (field file id 293) from the walkaway experiment with a vertical source offset 4 m from the northernmost sensor. Radial for this example is approximately positive north, transverse is approximately positive east vertical positive up. Note an oddity of the geometry is that the radial direction is approximately the longitudinal direction for a direct *P*-wave path.

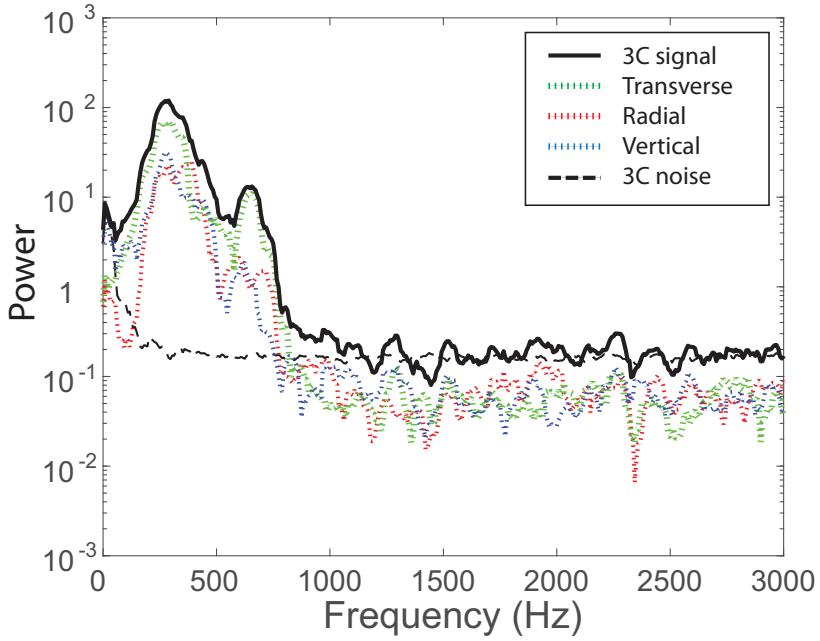

Figure 3. Power spectral estimates of signal and noise from sensor 20. Figure is a semi-log plot with the *x*-axis range limited to 0–3 kHz as there is no signal between 3 kHz and the Nyquist frequency of 4 kHz. Power spectral estimates for individual components are shown with coloured, dotted lines as defined in the legend. The heavy black line is the total three-component power produced by summing the three-component estimates. The noise power estimates (black dashed line) are similarly estimated by summing noise power spectra from the three components.

3 TRAVELTIME ANALYSIS

Wave speed variation with propagation direction was the first method used to argue for the existence of anisotropic wave propagation in the mantle (Hess 1964). Later work (Leven *et al.* 1981) showed these observations are well explained by preferred orientation of olivine in the upper mantle. The Homestake Mine was constructed to extract gold from veins intruding into the Homestake Formation. Noble *et al.* (1949) describe the Homestake Formation as 'sideroplesite schist with abundant pods of recrystallized quartz'. The foliation is oriented approximately parallel to axial planes of large recumbent folds (Noble *et al.* 1949) that permeate the mine over a range of scales (Fig. 4). Schists are known from experimental data (see landmark papers by Christensen 1965, 1966, and similar subsequent laboratory measurements) and theoretical calculations based on measurements of texture (CPO/LPO; e.g. Cholach & Schmitt 2006; Wenk *et al.* 2010; Erdmann *et al.* 2013) to be highly anisotropic and show large variations in *P*-wave speed with direction of propagation. Hence, we test the hypothesis that these

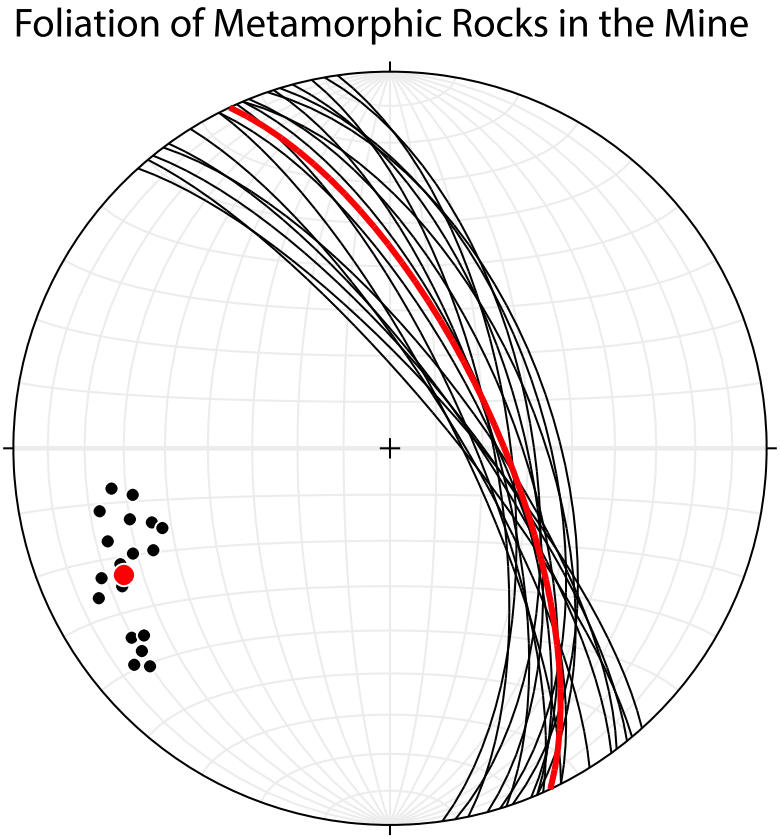

Figure 4. Lower hemisphere stereonet plot of the foliation measurements taken in drifts near the experiment. The data plotted were measured by geologists of the Homestake Mining Company in the early 1980s, preserved by SURF, and extracted by us from field scanned field maps. The black lines represent foliation planes, and the black dots are their corresponding poles. The red line and red dot are the average foliation strike/dip (334.8/67.3) and the average foliation pole, respectively. This plot was produced with Stereonet 10.0 (Allmendinger *et al.* 2011; Cardozo & Allmendinger 2013).

rocks are anisotropic by measuring *P*-wave velocity variations with azimuth.

We focused on the data from the fan-shot experiment for this analysis. The data from the walkaway experiment are of limited use to test this hypothesis, because the range of source-to-receiver azimuths with the geometry of the walkaway experiment is less than 10°, while that of the fan-shot experiment spans nearly 180°.

To measure traveltimes, we filtered the data with a three-pole Butterworth bandpass filter with corners at 100 and 500 Hz. We then picked first breaks by conventional interactive picking methods. Traveltime plots and common receiver gather sections demonstrated, however, that the data were subject to source timing errors. The instrument used a standard hammer switch designed for shallow seismic experiments. As noted earlier, surface data typically have a frequency content that is an order of magnitude lower than these data. With surface data the inaccuracies we uncovered (∼1 ms) would be negligible or absorbed in shot statics. Hence, we developed a custom method to deal with the shot time inaccuracies.

We used the standard mathematical model of static corrections. That is, we assume that the measured traveltimes can all be written as

$$t_{ij} = \tau_i + T\left(\boldsymbol{x}_i, \boldsymbol{x}_j\right), \tag{1}$$

where t_{ij} is the measured traveltime from source at position $\boldsymbol{x}_i$ to a receiver at position $\boldsymbol{x}_j$, $T(\boldsymbol{x}_i, \boldsymbol{x}_j)$ is the actual traveltime between these two points, and τ_i is the source static for shot i. For these data, τ_i is the timing error for shot i. Eq. (1) shows that if we have an estimate of $T(\boldsymbol{x}_i, \boldsymbol{x}_j)$ the shot statics can be computed as the simple average:

$$\hat{\tau}_i = \frac{1}{N_i} \sum_{i=1}^{N_i} \left\{ t_{ij} - \hat{T}\left(\boldsymbol{x}_i, \boldsymbol{x}_j\right) \right\}, \tag{2}$$

where $\hat{T}$ is an estimate of the true traveltime and N_i is the number of traveltime measurements for shot i.

We estimated the shot statics by a two-step procedure. The first was a grid search method where we assumed the true traveltime function could be written as

$$\hat{T}\left(\boldsymbol{x}_i, \boldsymbol{x}_j\right) = \left\| \boldsymbol{r}_{ij} \right\| / V_p \tag{3}$$

with $\|\boldsymbol{r}_{ij}\|$ denoting source–receiver distance and V_p denoting an assumed *P*-wave velocity. With that assumption we can compute the global misfit of all traveltimes with a single velocity value as:

$$\|\delta \boldsymbol{t}\| = \sqrt{\sum_{i=1}^{N_s} \sum_{j=1}^{N_i} \left(t_{ij} - \left\| \boldsymbol{r}_{ij} \right\| / V_p\right)^2}. \tag{4}$$

We determined an estimate of V_p as the value that minimized $\|\delta \boldsymbol{t}\|$. These data yielded a well-defined minimum at 6150 m s^{-1}, which is consistent with other measurements we made independently from the walkaway data using least square line fits to first break picked times and velocities measured using peaks in τ-p stacks. With an estimate of V_p the second step in our procedure was to estimate each of the shot statics by combining eqs (2) and (3). The

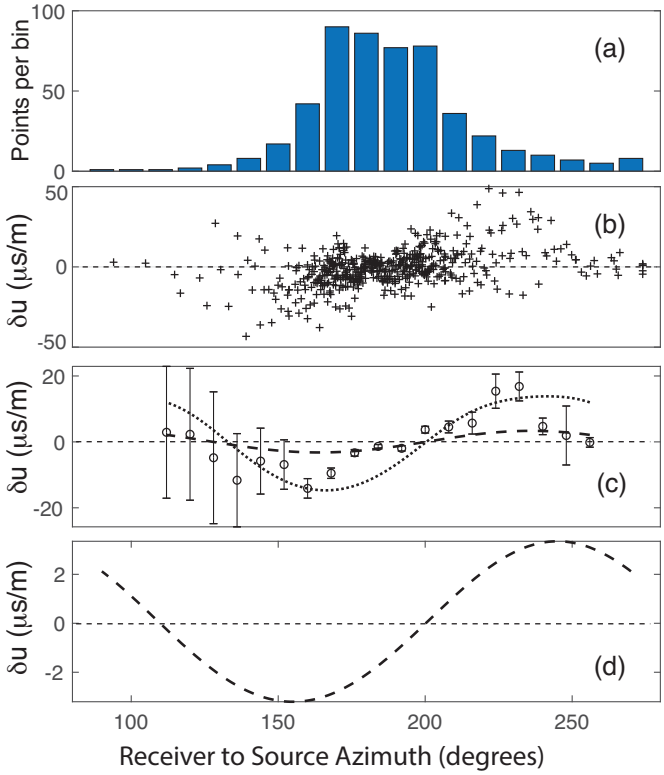

Figure 5. Slowness variations as a function of receiver to source backazimuth. (a) illustrates the number of points averaged in each azimuthal bin. (b) shows the raw data averaged to produce (c). (c) is the summary figure illustrating traveltime variations expressed as a slowness anomaly averaged in equal angle bins. Note that with the base velocity we used of 6150 m s^{-1}, the $+20$ μs m^{-1} point is 5476 m s^{-1} and -20 μs m^{-1} is 7012 m s^{-1}. The error bars are one standard deviation estimated as described in the text. The dotted line is the predicted slowness variation for the proxy schist with no fractures and the dashed line is the comparable variation computed for cracks oriented with the foliation planes. (d) shows the crack model variations alone with a 10x scale. It shows that the crack model variation has the same form as the LPO effect for this schist but is much smaller in amplitude.

static corrected times were then converted to slowness anomalies defined as

$$\delta\, u_{ij} = t_{ij} - \hat{\tau}_i - \frac{\|\boldsymbol{r}_{ij}\|}{\hat{V}_p}, \tag{5}$$

where $\hat{\tau}_i$ are the set of estimated shot statics and $\hat{V}_p$ is the P-wave velocity determined from the grid search method. The estimated statics ranged from -1.5 to $+3$ ms with a mean of 1.1 ms and a standard deviation of 1 ms suggesting the hammer switch is only capable of 1 ms precision.

The results of this procedure applied to the traveltime data are illustrated in Fig. 5. The average slowness estimates show a strong departure from zero consistent with an anisotropic medium. Fig. 5(b) shows a considerable scatter in the raw traveltime measurements, but there also exists a large redundancy as illustrated by the histogram in Fig. 5(a). We thus binned the data in overlapping bins spaced at 10° intervals with a range of ± 10° from the bin centre. For all bins with more than 6 data points we computed a confidence interval using a bootstrap method (Efron 1979). The centre of the distribution was defined from the median of the trials and the standard error was computed by scaling the interquartile range assuming a normal distribution. For bins with smaller numbers of points, we used a more conservative propagation of error method. The static estimation procedure results and the inspection of linear misfits both suggest that the picking uncertainty is around 1 ms. If we assume an average offset of 50 m then the projected uncertainty when a time is converted to slowness is $\sigma_{\delta u} = 20$ μs m^{-1}. The uncertainties in μs m^{-1} are then estimated for points with low degrees of freedom as $\sigma_{\delta u} = 20/\sqrt{N}$, where N is the number of points in the bin. The left four bins in Fig. 5(c) are the only ones using this method. The results suggest the estimate may be overly conservative, but we suggest that is a preferable approach for the most poorly constrained points. In contrast, a bootstrap naively applied to a single point would yield an uncertainty of zero, which is obviously not correct. Similarly, sets of points with low degrees of freedom can easily yield unrealistically small uncertainties by chance. In any case, Fig. 5 demonstrates that the traveltime data show statistically significant variations, as defined by the error bars, with azimuth. In the next section, we describe the way we computed the petrologic model result plotted in Fig. 5.

4 MODEL FOR AZIMUTHAL VARIATIONS FROM SCHIST ELASTIC TENSOR

We modelled the azimuthal variations in compressional wave speed and P-wave particle motion variations using an elastic tensor estimated for a schist sample from southeast Vermont. We used this sample as a proxy because we had no sample of the actual rock at the field site. We chose this sample from a collection of samples from an unrelated, ongoing project on the Chester Dome. The sample chosen has similar mineralogy and texture to descriptions of the Homestake Formation given by Harder & Noble (1948), but with some important differences. The model schist is metamorphosed

at higher-grade conditions and has a larger average grain size. The carbonate within the model schist is $CaCO_3$ rather than $FeCO_3$, $MgCO_3$, and the sample used here did not have carbonate. Harder & Noble (1948) suggest the Homestake Formation also has significant graphite in some areas, which is not widely present in the model schist. Despite these differences, we expect the patterns produced by the model schist tensor to be a good analogue to those of the Homestake schist because mica-rich rocks generally have similar patterns of anisotropy (Brownlee *et al.* 2017). The elastic tensor for the model schist was calculated from electron backscatter diffraction (EBSD) characterization of mineral crystallographic preferred orientation (CPO). This method combines single crystal elastic tensors with CPO data for each mineral phase first to calculate single mineral aggregate tensors, and then to calculate a bulk aggregate tensor by averaging the single mineral aggregate tensors according to the volume proportions of the minerals in the sample.

To model the azimuthal variations in observables we used a solution to the Christoffel equation:

$$\left|C_{ijkl}\langle X_i X_j\rangle - V^2 * \rho * \delta_{ik}\right| = 0$$

where C_{ijkl} is the elastic tensor, X_i and X_j are the direction cosines, V are the seismic phase velocities, ρ is the density and δ is the Kronecker delta. The seismic phase velocities and particle motion vectors are solved for any possible propagation direction. We solved for directions covering a full sphere at every degree in polar coordinates. To compare predictions directly to observations, we rotated the elastic tensor to the average orientation of the foliation of the Homestake Formation within the mine. Fig. 5(c) shows this model is consistent with the general pattern of the velocity variations. The actual curve fit, however, would be marginal for any statistical test using the estimated uncertainties.

Fig. 5 also shows results for modelling the influence of fractures. We assume fractures are aligned with the foliation direction defined by the average plane illustrated in Fig. 4 (strike 335° and dip 68°). We used a crack aspect ratio of 1 (circular fractures), which assumes fractures will not contribute to anisotropy within the fracture plane. We used isotropic background velocities corresponding to the analogous schist sample, 5920 and 3510 m s^{-1} for *P* and *S* waves, respectively, and a Hudson crack model with fill material of the same isotropic properties as the background and a crack density of 0.04 as inputs for the MS_effective_medium fracture modelling code that is part of the MSAT package (Walker & Wookey 2012). Figs 5(c) and (d) demonstrate that with the assumed fracture density and orientation the impact of fractures is negligible compared to the influence of preferred orientation of minerals. Related modelling, however, suggests that with higher fracture densities and different fracture orientation it is feasible to produce velocities as low as 4500 m s^{-1} from a 6150 m s^{-1} ($\delta u = 60\ \mu s\ m^{-1}$) background. Higher fracture densities may be present in the damage zone around the mine drift. We discuss the potential existence of lower velocities near drifts below as that possibility has more importance to particle motion measurements than traveltimes.

5 PARTICLE MOTION MEASUREMENTS

5.1 Coordinates

The traveltime data confirm our hypothesis that this experiment was conducted inside an anisotropic medium. In this section, we describe three methods we used for estimating *P*-wave particle motions and the results of applying them to these data. Particle motions are, by nature, 3-D tracks sometimes visualized by hodograms. Furthermore, anisotropic properties by definition have orientation properties. Hence, we need to define the set of coordinate systems that we used to define particle motions and/or the orientation of the medium. Fig. 6 illustrates the geometry used in this paper. Our rotated coordinate system is a variant of what is sometimes called LQT coordinates (Reading et al 2003; Svenningsen & Jacobsen 2004). It is a variant because our association to the set of x_1, x_2, x_3 in Cartesian coordinates is in a different order than the corresponding axes of LQT, so we refer to our coordinate system as TQL to emphasize that order. The figure also defines two angles, ϕ and θ, with a stereographic projection. Those angles are important as we use them to parametrize *P*-wave particle motion deviation estimates in figures below. Fig. 6 also defines the backazimuth angle, ϕ_{baz}, that is used as the independent variable in particle motion deviation plots. We emphasize that ϕ and ϕ_{baz} are fundamentally different; ϕ is an angle that characterizes a unit vector direction in the TQL system while ϕ_{baz} is an angle used to compute the transformation matrix that transforms the data from geographic orieintations (ENZ) to TQL.

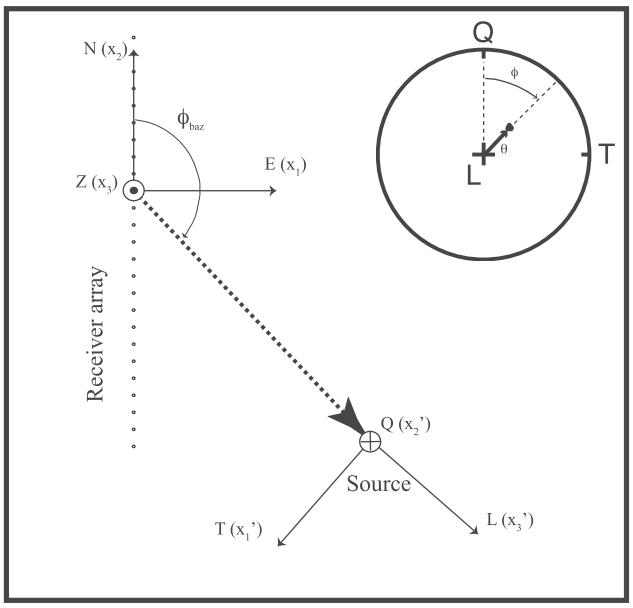

Figure 6. Coordinate definitions. The figure shows the geometry of the TQL coordinates by transformation of the original geographic coordinates. The small row of dots illustrate the sensor array location for this experiment. The dashed line with the arrow defines backazimuth. The inset figure in the upper right is an upper hemisphere stereographic projection that defines the angles ϕ and θ in the TQL system.

5.2 Methods

5.2.1 Time-domain methods

Two of the approaches we used to measure *P*-wave particle motions directly manipulate the vector motion defined by a three-component seismogram. The first is conceptually similar to the transverse component minimization method used to measure shear wave splitting, which was introduced by Silver & Chan (1991). The method was based on the principle that the direction of any three-component unit vector can be described by two angles, θ, φ, that define the

grid search range. We extracted a time window from the first break time and some specified end time. In this paper, we aimed to use the first cycle of the *P* wave, which we estimated as 2 ms. We then rotated the three-component data by all reasonable values of angles θ, φ to determine what angle pair maximized the ratio of energy on the longitudinal component to the norm of the energies on all three components of the particle motion vector.

The second time-domain technique was a principal component approach using a singular value decomposition (SVD) following the method introduced by Jurkevics (1988) and probably the most commonly utilized method for estimating *P*-wave particle motions (e.g. Fonaine *et al.* 2009). In our case we used the data from the same time window as the grid search algorithm and assembled the data into a Nx3 matrix, which we will call $\boldsymbol{D}$. We then performed a singular value decomposition of $\boldsymbol{D} = \boldsymbol{USV}^T$. As shown by Jurkevics, the right singular vector associated with the largest singular value can be used to define the direction of principal *P*-wave polarization over that time window.

5.2.2 *Multiwavelet method*

The concept of multiwavelets was introduced by Lilly & Park (1995) for particle motion estimation and extended by Bear & Pavlis (1997, 1999) and Bear *et al.* (1999) to three-component seismic array processing. The array methods are not appropriate for this paper, however, because the waveforms vary rapidly across the array of sensors. Hence, the methods we used are a variation of those in Lilly & Park (1995).

Multiwavelets are a form of wavelet transform (e.g. Strang & Nguyen 1996). Applications of wavelet transforms have grown to a huge field since the time of the original Lilly & Park (1995) paper on multiwavelets. Lilly and Park coined the term multiwavelet, but evolution of the field has led to a confusion of the terminology. Lilly and Park used that term because of a relationship to multitaper spectral method. Outside of seismology, however, 'multiwavelet' has been adopted to mean something different. A wavelet transform can be implemented by convolution of an input time-series with a series of filters. Consequently, some forms of the wavelet transform, including what we are calling the multiwavelet method, can also be a called a filter bank. The output of the filter bank can be used to appraise scale dependence of a derived parameter. Appraising scale dependence is what 'multiwavelet' has come to mean in other fields. The wavelets we used, however, are unusual. We are aware of no applications of the technique outside of seismology. The wavelets we use are special, narrowband filters with a close association to multitaper spectral methods. Consequently, it is necessary to provide a more extensive theoretical background. We elected to relegate the mathematical details to the Supporting Information with the intent of keeping the text focused on the scientific problem, rather than the technical details of a method introduced in earlier literature. The Supporting Information is a necessary documentation for this paper, however, as our implementation differs in many details from the original work by Lilly & Park (1995). In this subsection, we focus primarily on the fundamentals of the method and how multiwavelets complement the methods described in the previous subsection.

The first distinction of the multiwavelet method from the other wavelet methods, is that the multiwavelet method is a hybrid time-domain and Fourier transform method. It is time-domain like because the method convolves a set of wavelets with the input data (the filter band concept) to yield a set of (complex valued) seismograms that are analysed to produce particle motion estimates. It has elements of Fourier transforms because the wavelets we use are the kernels of the multitaper spectral method (Thomson 1982). That is, the functions we use in our analysis are of the form

$$\begin{aligned} w_i(t) &= s_i(t)\, \mathrm{e}^{-\mathrm{i}\omega_c t} \\ &= s_i(t)\,[\cos\,\omega_c t + i\,\sin\,\omega_c t]\,, \end{aligned} \tag{6}$$

where $s_i(t)$ $i = 1,\ 2,\ \ldots,\ N_w$, are a set of Slepian functions that are parametrized by the time-bandwidth product and the length of the analysis window (Thomson 1982). The centre frequency of the wavelet set, ω_c, is constrained to be an integer multiple of the window length: $\omega_c = 2\pi n/T$ where T is the analysis window length. Note the wavelets defined by eq. (6) differ from those defined by Lilly & Park (1995) that they call 'Slepian wavelets'. Lilly and Park noted the alternative of eq. (6), but their original paper was focused on Slepian wavelets and mention this form only in passing. We have experimented with both choices but choose the multitaper kernel form in eq. (6) because the wavelets all have a linear phase by definition. We found that Lilly and Park's Slepian wavelets distort the phase with time. Since particle motions are strongly phase dependent we have elected to use only the form in eq. (6) for this analysis.

A key property of multiwavelets is that the functions in eq. (6) are orthogonal. As a result, when they are convolved with an input seismogram we obtain N_w statistically independent, complex-valued seismograms. The primary value of these seismograms is as a means to accurately measure time–frequency localization of phase. As we show in the Supporting Information, when a three-component seismogram is transformed with the wavelets in eq. (6), we can reconstruct a particle motion ellipse estimate from each wavelet at every time step. What is perhaps more important is the fact that the statistically independent noise sampling of the Slepian functions further provides a means to objectively estimate uncertainties in the particle motion ellipses at each time step. Previous implementations of multiwavelets by Bear & Pavlis (1998, 1999) and Bear *et al.* (1999) used a nonparametric method called the jackknife to estimate uncertainties. With advances in computing speed, for this paper we were able to use the more computationally intense bootstrap method to estimate uncertainties.

A second strength of the multiwavelet method is the ability of the method to test for possible frequency dependence of particle motion. This can be achieved by the infinite array of choices possible with eq. (6) or more efficiently by the scaling approach that defines what a multiwavelet is in the broader scientific community. In this paper we use the scaling approach with the same base wavelets applied to data downsampled by a factor of two. Here we used a mother wavelet defined by eq. (6) with a time-bandwidth product of 4 for which $N_w = 8$ with $f_c = \omega_c/2\pi = 400$ Hz (4 cycles in a 10 ms window). We generate a complimentary result for f_c= 200 Hz from the data downsampled by 2 (20 ms window).

The main negative of the multiwavelet approach relative to the methods described in the previous section is best seen in Fig. 7. That is, the wavelet functions have a finite duration and the output of the convolution is, by definition, a weighted average of the original data over the time spanned by the wavelet. For these data, in particular, Fig. 7 shows the wavelet we use spans a time period as long or longer than the time between the *P* and *S*. Because that time period is always less than or equal to the duration of any of the wavelets, we found it necessary to apply a tail mute at the *S*-wave arrival time. That was necessary to keep the larger amplitude *S*-wave signal from dominating the particle motion estimates for all but the largest offset. The mutes were applied from an *S* time computed

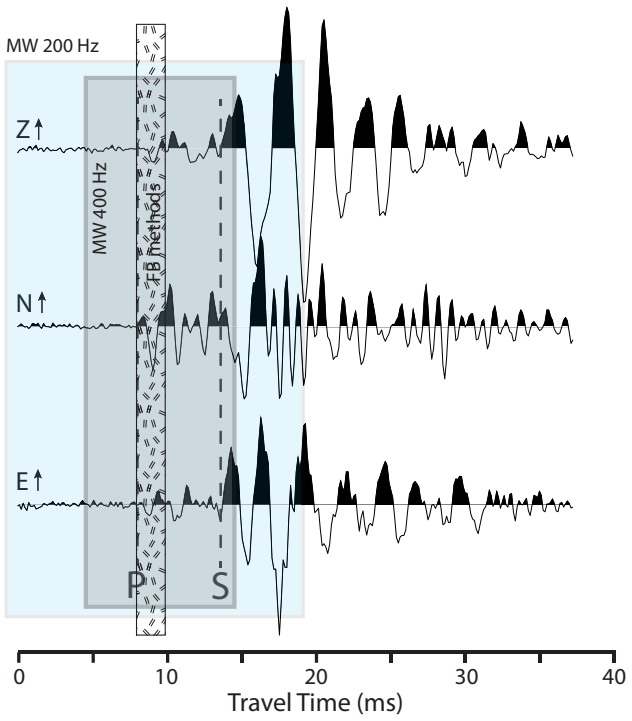

Figure 7. Comparison of analysis window lengths for different particle motion estimates. Windows are illustrated by translucent rectangles spanning the range of the analysis. The first break methods (grid search and SVD) use the window defined by the short hatched rectangle. The multiwavelet windows are illustrated in translucent blue for 200 Hz and translucent grey for the 400 Hz wavelets.

with a constant velocity of 3500 m s^{-1} with a linear taper length with a length of 4 ms starting 2 ms before the estimated *S* arrival time. The estimates of *P* particle motion for each seismogram were then computed with the *mwpmavg* program (see the Supporting Information) using a 2.5 ms long window beginning at the first point where the signal to noise ratio exceeded a factor of 3. Although that window is comparable to that for the first motion methods, the actual range over which the solution is averaged is always larger for the multiwavelet method. A pragmatic view of this for this paper is that one should view the multiwavelet results as an average for the entire *P* signal while the other methods focus only on the first cycle of the *P* wave.

5.3 Results

Figs 8 and 9 show results for the *P*-wave particle motion deviations in relation to theoretical predictions for the proxy schist used in Fig. 5 to model the slowness measurements. Fig. 8 shows all the particle motion estimates and bin averages computed by a similar algorithm to that used for the traveltimes (Fig. 5). The details of the averaging scheme are described in the Supporting Information, but a critical point is that the averaging uses a robust M-estimator method for the averaging with the estimate of centre computed from a weighted average of data. The base weighting uses the reciprocal of the uncertainties estimated from the multiwavelet analysis. For the first motion methods the initial weights are constant. We emphasize this point because one might think the results shown in Fig. 8(d) are wrong for the azimuth range of 140°–200°. The solution is not on the centre of the cloud of points because the robust solution properly downweights the points with larger angles accounting for the fact that the uncertainties are higher. The comparable averaging for the first motion estimates is not possible because there are no comparable uncertainty estimates for each point. This may partly explain some of the differences in the results of the different methods. All the average curves in Fig. 8 include uncertainty estimates computed by a bootstrap method applied to data in each azimuth bin as described in the Supporting Information. The uncertainties are important because they demonstrate that for all methods we used there is a statistically significant variation of *P*-wave particle motion with azimuth. Furthermore, if the media were isotropic, θ would average to zero. Every single estimate is statistically different from zero confirming the inference from the traveltimes that these rocks are anisotropic.

In Fig. 9, we plot the average curves for all methods. We plot the curves without the error bars to reduce clutter, but the error bars are shown in Fig. 8 for the total deviation angle θ. In Fig. 9(b), we also plot the azimuthal angle, ϕ, defined in the stereonet insert of Fig. 6. ϕ is a potentially useful observable for an anisotropic medium, but is undefined for an isotropic medium because the particle motion for pure longitudinal motion has no projection in the TR plane. For the same reason ϕ is an unstable measurement because a simple propagation of error formula shows that the uncertainty of ϕ scales as

$$\delta\phi = \frac{\delta\theta}{\sin\theta}, \tag{7}$$

where $\delta\theta$ is the uncertainty in θ (error bars in Fig. 8). As a result some of the errors predicted by eq. (7) in Fig. 9(b) are large when θ is small. The fact that we still see a smoothly varying pattern in Fig. 9(b) suggests the propagation of errors formula is overly conservative, but because of this inherent instability the results in Fig. 9(b) should be viewed with caution.

Fig. 9 also shows the predicted *P*-wave deviation for the same proxy schist model discussed in Section 4. Figs 9(a) and (b) plot the model predictions as a function of the independent variables θ and ϕ we use to parametrize the unit vectors that are the actual observable.

The agreement of the particle motion data to this model is poorer than the fit to the traveltime data. All the measurements show a general cyclic pattern over a range of 180° as expected for an anisotropic medium. Fig. 9(a) shows that the multiwavelet pattern is similar to the model predictions, but is offset by +20°–30° and differs in amplitude by at least a factor or 2. The first motion and multiwavelet methods agree within the error bars between backazimuths of 130° and 200° but both first motion methods yield much larger angle estimates for backazimuths over 200°. Note, however, that the sample size is much smaller for angles larger than 200° so that difference may be a sampling artefact. Fig. 9(b) shows predicted ϕ angles for the proxy schist with uncertainties computed by assuming errors in the orientation of the foliation plane. ϕ is extremely dependent upon that quantity as ϕ becomes undefined and the errors become unbounded when particle motion is longitudinal ($\theta = 0$). ϕ is predicted to vary rapidly with angle and our measurements are reasonably consistent with the model given the large error bars.

Overall, given that our model is not based on actual Homestake Formation rocks but a proxy and the local foliation direction is inferred from routinely measured mine records, we suggest the fit is better than might be expected. The data demonstrate the medium is unambiguously an anisotropic medium with statistically significant deviations of *P* particle motion from what would be expected for an isotropic medium. The smoothly varying pattern shows the expected

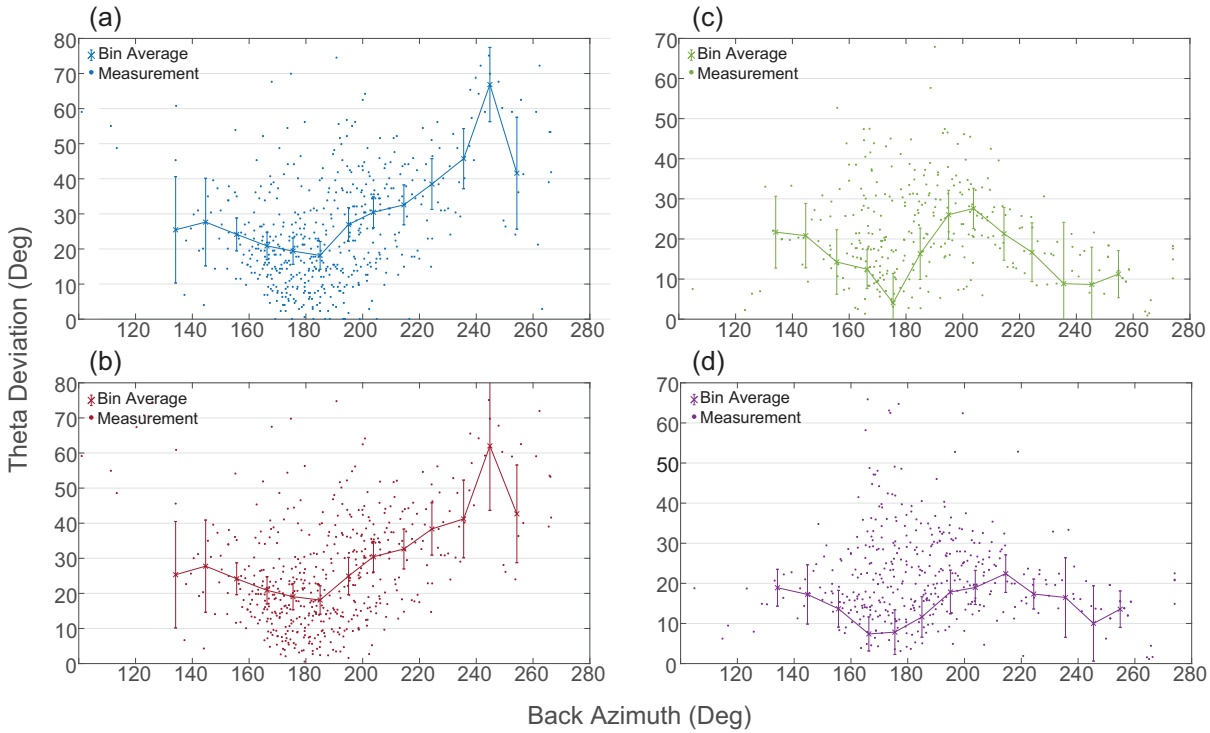

Figure 8. *P*-wave particle motion results for all methods. All plots are the total deviation from longitudinal angle, θ, as a function of receiver–source backazimuth (see Fig. 6). All figures show raw single sensor measurements as dots. Bootstrap averages are displayed as an x symbol connected by lines. Vertical lines are 95 per cent confidence intervals. Parts (a)–(d) are results for the grid search, SVD, 400 Hz multiwavelet, and 200 Hz multiwavelet solutions, respectively.

approximately 180° cyclic pattern for any anisotropic medium consistent with the measured foliation. The reason the fit of the model to the data is poor compared to the traveltime data is not clear but may be a result of additional complexities we discuss next.

6 DISCUSSION

The first-order conclusion of this paper is that the Homestake Formation within the study area on the 4850 level of the mine is unambiguously an anisotropic medium. Both the traveltime data and multiple methods of measuring *P*-wave particle motion are consistent with patterns predicted from a lattice preferred orientation model for a proxy schist. The fit of the data to the model is significantly better for the traveltime data than the particle motion estimates. To the best of our knowledge this is the first direct validation of lattice preferred orientation induced anisotropy at the 10–100 m scale. The 'direct' qualifier in the previous sentence is necessary because many papers have been published in the last decade that infer anisotropy at a larger scale but depend upon an inversion algorithm to attempt to separate average wave speed variations from anisotropic properties (e.g. see reviews by Fouch & Rondenay 2006 and Romanowitz & Wenk 2017). Alternatively, numerous observations in the oceans (e.g. Shearer & Orcutt 1986; VanderBeek & Toomey 2017; Mark *et al.* 2019) have confirmed the original discovery by Hess (1964). Those observations are widely accepted as due to a coherent fabric in the upper mantle at the scale of 100 s of km that allow these studies to make an inference from a path averages for such a large distance. A unique feature of our results is that the homogeneous, anisotropic solid assumption is not absurd as it would be at a larger scale in the continental crust. The results suggest, however, that the homogenous assumption is suspect even at this smaller scale. We would argue that it is important to consider this issue as it has fundamental importance for the way heterogeneity at a range of scale lengths impact observables as discussed by Okaya *et al.* (2019).

The traveltime data have a reasonable fit to the homogenous anisotropic model given the model is completely independent and based only on a proxy. This was possible in spite of the fact that the uncertainties in individual measurements are high. A subtle issue not universally appreciated by seismologists is that with fixed bandwidth data reducing source–receiver offset can lower the precision of wave speed estimates. The reason is a simple error propagation issue; slowness is time divided by distance so with a fixed picking uncertainty slowness errors become unbounded as distance goes to zero. From repeatability tests and scatter of the data in Fig. 5(b) we estimate the picking uncertainty of these data is of the order of 1 ms. The data illustrated in Fig. 5 have offsets of 20–100 m. With a nominal *P*-wave speed of 6000 m s^{-1} that translates to uncertainties ranging from 5 to 20 per cent. We are able to see through such a high uncertainty only because the experimental geometry provided enough redundancy to reduce the uncertainties of the average enough to resolve the pattern seen in Fig. 5(c). Because the bootstrap and propagation of error predict similar uncertainties the slowness deviation values are unambiguously different from zero. The results also show a pattern as a function of backazimuth that is definitely not random.

The *P*-wave particle motion data have a more complicated relationship because we used multiple estimation methods and the measurements utilize more of the waveform than a simple traveltime pick. As illustrated in Fig. 7 the two approaches we called the first motion methods use approximately the first cycle of the *P* wave. The multiwavelet estimates for these data in both frequency bands need to be viewed as averages of the entire *P* waveform. An

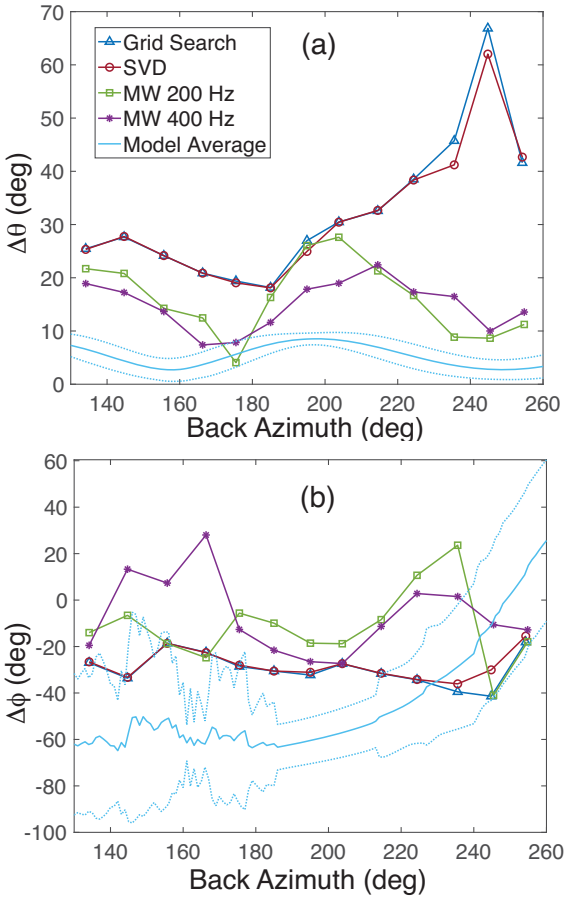

Figure 9. Comparison of *P*-wave particle motion estimates by different methods. (a) is directly comparable to Fig. 8 but we omit the error bars to reduce clutter. We also plot theoretical predictions from the elastic tensor method as a solid blue line with the label 'Model average'. The blue dashed lines are the standard deviation computed from an ensemble of models produced by random resampling of the strike and dip of the foliation plane. The resampling used a strike of 335° ± 10° and dip 68° ± 7°, which are the mean and standard deviation of the strike dip measurements illustrated in Fig. 4. These error estimates neglect uncertainties in elastic properties and are thus lower bounds. (b) shows measured variations by all methods in the azimuthal angle deviation, ϕ, defined in the stereonet portion of Fig. 6. We again omit the error bars to reduce clutter but note the errors are proportionally larger than those illustrated for θ in Fig. 8 by a factor of $\csc\theta$ (approximately a factor of 4 with a nominal scale of ±20–30°). Errors in ϕ estimates are thus infinite when $\theta = 0$. As in part 1 the solid blue line is the average from trials and the dashed lines are standard deviation of trials with random resampling of strike and dip.

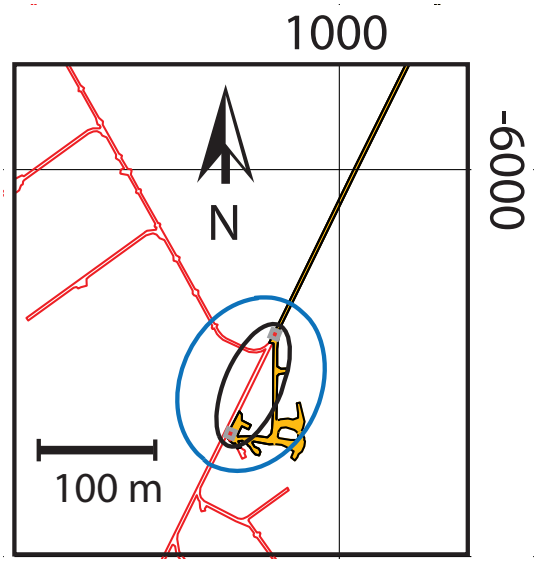

Figure 10. Scale of scattering ellipses for particle motion estimates. Background is a map of drifts on the 4850 level of Homestake. Lines show survey positions in mine coordinates. The yellow areas are the same as in Fig. 1 where the location of sources and receivers are illustrated. The red lines are mine drifts that exist but are currently closed to access. Two ellipses are drawn with red dots marking the foci at source and receiver positions separated by 100 m. The black ellipse is the outer limit of *P* scattering for the first motion methods and the blue ellipse is the comparable ellipse for the multiwavelet methods. Both ellipses were computed using a *P*-wave speed of 6000 m s^{-1} and a source–receiver separation of 100 m.

understanding of how this compares to traveltimes is illustrated in Fig. 10. In the standard theoretical model, we view traveltimes as integrating velocity along a 'ray path', which in this case is well approximated as a straight line between source and receiver. The textbook justification for this (e.g. Aki & Richards 1980) is that the first arrival is the minimum time path from source to receiver. An observable measured using a finite time window, in contrast, can be influenced by scattering inside a finite volume. The volume involved is constrained by the traveltime difference between the longer path defined by *P* to *P* scattering and the direct wave. For a constant velocity medium it is easy to demonstrate that the feasible scattering volume can be described by an ellipsoid of revolution. The foci of the ellipsoid are the source and receiver position. Its extent is defined by the time difference between the end of the window and the *P*-wave arrival timescaled to distance by the *P*-wave speed. Fig. 10 illustrates horizontal sections through the largest such ellipsoids that are feasible for these data. The ellipses illustrate that the largest volume that can contribute to variations in the *P*-waveforms is of the order of 10 m from the ray path for the first motion methods but of the order of the scale of the receiver array for the multiwavelet analysis. The volume this represents is not trivial, but the most important thing it emphasizes is that for these data we can absolutely neglect the influence of mine works outside a volume of the order of 100 m.

Fig. 10 shows there are several mine drifts on the 4850 level that could potentially be influencing the particle motion measurements by all methods, but especially the multiwavelet results. Furthermore, in the Supporting Information we include a 3-D PDF that can be used to view other drifts above and below 4850. In this area the mining company constructed drifts about every 50 m in depth, so there are at least two additional sets of drifts not illustrated in Fig. 10 that might influence the data. As the 3-D figure illustrates the drifts at other depths have a similar geometry to that on 4850 in this area. On the other hand, this was not an area of active ore removal but an access tunnel to an ore body Homestake geologists called 19-ledge located south of this location. Mining voids were backfilled with tailings and if present would strongly scatter seismic waves due to the strong contrast in material properties. The scattering ellipse geometry in Fig. 10 shows scattering from backfilled mine voids can be dismissed as a problem for the *P*-wave particle motion data. It could, however, potentially be an issue with *S*-wave data and could explain why we had difficulty working with the *S*-wave data.

A related issue for the particle motion results is the potential influence of fracturing in the vicinity of the drifts. Fracture densities are likely higher near mine drifts because they were constructed using explosives, although the distance scale where this occurs is unknown. Open fractures tend to reduce wave speeds, so we would thus expect wave speed variations in the vicinity of the drifts. A tomographic experiment by Roggenthen & Berry (2016) in a different area of the 4850 level suggest this could be the norm, although their measurements were made in an amphibolite unit and are not directly comparable. Fracture model calculations we made (Section 4) suggest that reduction of *P*-wave speed to less than 5500 m s^{-1} require unrealistically high fracture densities. Using a lower bound of 5500 m s^{-1} a simple Snell's law formula predicts a maximum deflection of the propagation direction of 25° from a reference of 6150 m s^{-1}. This may explain part of the large offset in the measured particle motions relative to that predicted from the petrologic model. However, the same simple refraction model suggest the skin depth of any velocity reduction near the mine drifts cannot be more than 1–2 m or we would observe a bend in the traveltime curves with slower wave speeds at the near receivers. In this entire experiment we collected hundreds of records like Fig. 3 (see the Supporting Information) and never observed a *P*-wave traveltime curve that could not be fit by a single line. Hence, although there likely is a damage zone that impacts wave speeds near the walls of the drift it cannot be very thick. One possible explanation for the difference in particle motion deflections for the first motion methods and the multiwavelet methods is that the first motion methods are higher frequency and more subject to near field effects from the damage zone.

Fig. 11 provides additional insight on this issue. There we plot the total deflection angles observed from the walkaway experiment, but averaging data for each receiver. Because the walkaway experiment azimuth range is only a few degrees, the results for all sensors should be statistically indistinguishable. That is not the case. We see large and systematic deviations with location. The variations are especially striking and systematic for the higher frequency, first motion methods. The results in Fig. 11 suggests the homogeneous anisotropic assumption is almost certainly wrong and there are large variations in properties from a superposition of LPO/CPO and fracture induced anisotropy that is strongest near the mine drift.

This lengthy discussion of possible sources of scattering has proven necessary because of complexities in these data that we found surprising. Our hypothesis in designing the experiment was that because these were metamorphic rocks at a significant depth they would be relatively transparent to seismic waves. We made that hypothesis based on extensive evidence from deep seismic reflections experiments. Since the earliest days of COCORP making sense of the limited returns from reflection experiments conducted over basement rocks that are predominantly anisotropic metamorphic rocks has been a challenge (e.g. Oliver *et al.* 1983). The record section shown in Fig. 3 and other record sections seen later in this paper demonstrate that there are large variations in waveforms even between adjacent sensors (4 m intervals). The variations were so huge we initially feared we had large numbers of scrambled channels, but we found that was not true at all. We produced Fig. 12 to provide a perspective for this discussion. This figure shows the scale of seismic wavelengths in the bandwidth of these data relative to the scale of inhomogeneities we were aware of that are potentially relevant. It is similar in concept to fig. 2 of Okaya *et al.* (2019) that is an important sidebar for this discussion. Fractures are not illustrated because attempting to place fracture geometry in this format would be misleading. The reason is the issue of aspect ratio. The lower

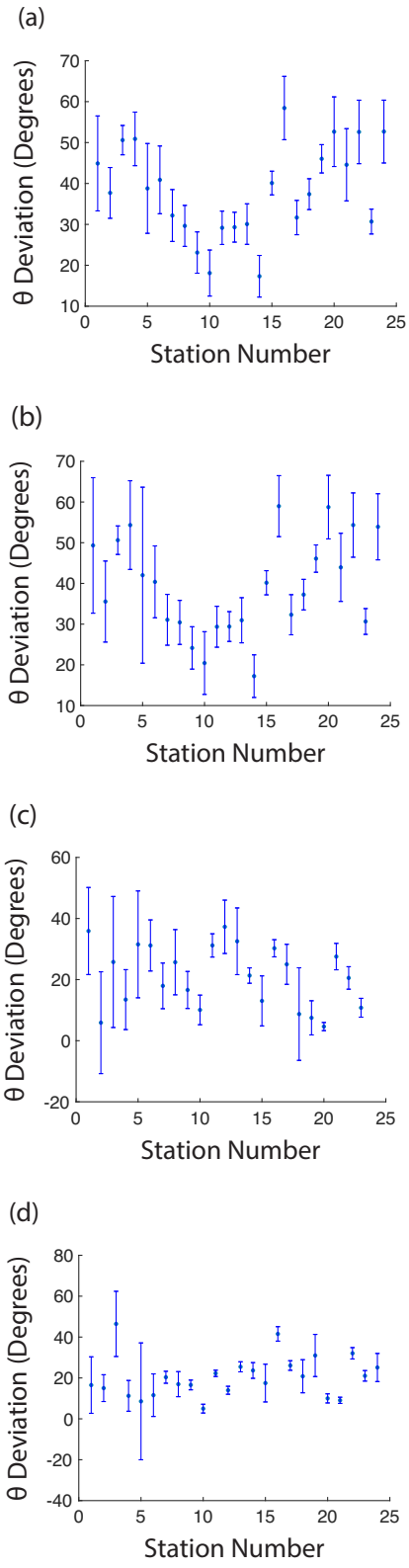

Figure 11. *P*-wave particle deviations from walkaway experiment. Plots show bootstrap mean and confidence intervals computed by averaging data grouped by sensor. Order is the same as Fig. 9: (a) grid search, (b) SVD and (c and d) multiwavelet estimates at 400 and 200 Hz, respectively. The *x*-axis is station number (Fig. 1), which is equivalent to a distance along the receiver array. Error bars are 95 per cent confidence intervals computed as described in the Supporting Information.

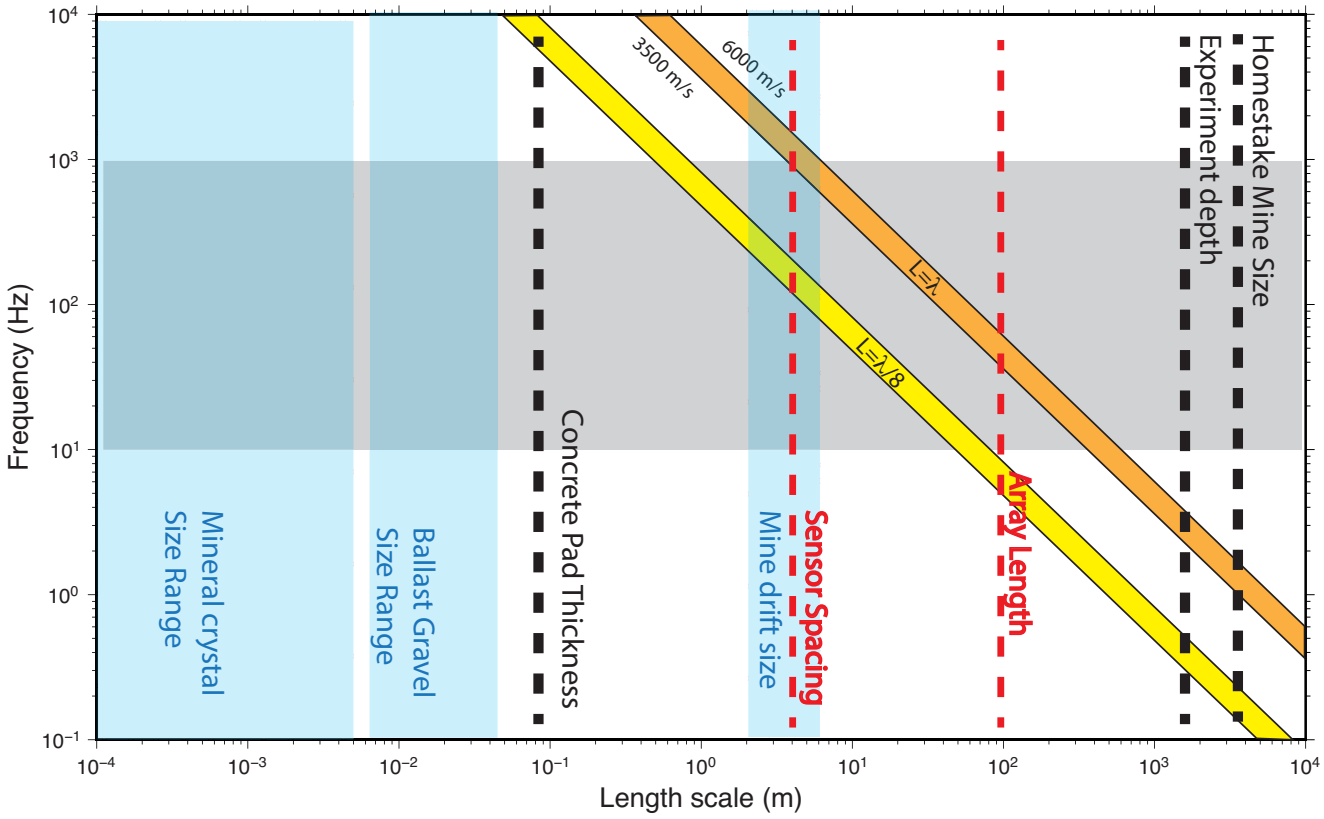

Figure 12. Illustration of scale variations in heterogeneities that could influence *P* particle motion data. Plot is a log–log plot with scale lengths on the *x*-axis and frequency of seismic waves on the vertical axis. The frequency content of these experiments span the grey region. Blue bands are size ranges for different heterogeneities discussed in the text. Note drift size scaling shows only the cross-drift scale. Many mine drifts at Homestake are km length scales along their axis. Features with a fixed or more limited range of scales are shown as dashed lines. The orange and yellow band shows the scaling relation of one and 1/8 of a seismic wavelength respectively to frequency following Okaya *et al.* (2019).

bound on fracture size is the opening width, which at this depth is likely on the scale of microns. The long axis scale of a fracture, however, can vary from microns to 100s of m or more. Hence, the range of fracture scale could be illustrated as painting nearly the entire range of Fig. 12.

Fig. 12 suggests three competing hypotheses that could contribute to the complexity we observe: (1) scattering by heterogeneity created by mining, (2) intermediate scale (1–100 m scale) variations in elastic properties and (3) scattering by fractures. A fourth hypothesis that is a variant of (1) is resonances and/or scattering by irregularities in the mine drift walls. The scattering hypotheses (items 1–3) are all possible and cannot be rejected without additional information not currently available to us. We discussed the viability of mining void scattering above. Intermediate scale heterogeneity is also viable. Roggenthen & Koch (2013) used well logging techniques to measure wave speeds at Homestake and found wide variations in *P*-wave speed from 4500–7000 m s^{-1} and *S*-wave speeds ranging from 2500–4000 m s^{-1}. Their data show there are significant variations in the rocks at Homestake on the 1–100 m scale. Any method to model elastic wave scattering (reflection is a special form of scattering) will show that variations of wave speed of the scale Roggenthen & Koch (2013) measured can generate significant scattering. Unfortunately, we have no data to directly measure properties at the required scale within the area of this experiment. We used an anisotropic model to fit the traveltime data (Fig. 5), but as argued earlier most of the scatter in the slowness estimates in Fig. 5 can be explained by picking errors. We would argue that an inversion to attempt to separate lateral variations in wave speed from anisotropy would fail due to the short path lengths and limited number of possible picks. Finally, the influence of fractures cannot be dismissed outright either. Numerous examples exist in the literature that link scattering observed in full waveform sonic logs to fractures (e.g. Lefeuvre *et al.* 1993; Beckham 1996). Such studies show recorded signals in the vicinity of borehole fractures can vary dramatically on short distance scales. We suggest these data may be subject to a similar local site phenomenon where an individual sensor's response is distorted by nearby fractures. Imagine, for example, a sensor floating on a block isolated by nearby fractures. This hypothesis could be tested with additional experimental data, but not with these data.

Resonance is one hypothesis that we can demonstrate is important in these data. The spectrum shown in Fig. 3 for sensor 20 is an example. That sensor shows a strong peak seen only on the transverse component at a frequency around 700 Hz. Most spectra we have examined show similar peaks on individual components. The inconsistency from channel to channel show that the peaks are not a resonance problem with the sensors we used. Fig. 13 shows the most extreme resonance example in the data set. The record section part of the figure shows an obvious ringing on transverse on sensor 7 compared to sensor 8. We also plot an average spectral ratio between the transverse components for these two sensors. If these two sensors recorded nearly identical signals as we would expect, the ratio should be flat. The results are far from flat with a peak at

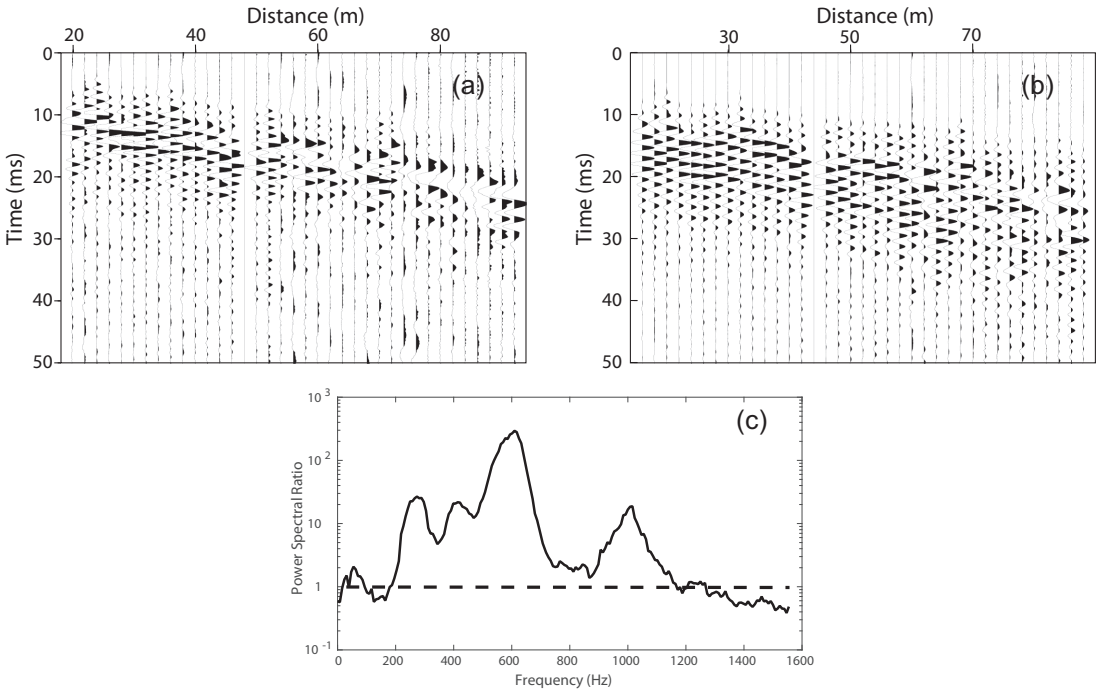

Figure 13. Example of resonance in Homestake data. (a) and (b) are common receiver gathers of transverse components (EW) plotted as a function of source–receiver offset for sensors 7 and 8, respectively. (c) is a semi-log plot of the median spectral ratio of all sensor 8 transverse signals divided by sensor 7 transverse signals for the same shot. The dashed line defines the baseline for a spectral ratio of one which would be the case if the two signals were identical. Spectra were computed by the multitaper method with a time bandwidth product of 4.

600 Hz having power 2 orders of magnitude larger on 7 compared to 8. Note in Fig. 1 that sensor 7 is located near a cavity in the side of the drift. That association suggests the observed ringing may be linked to a free mode of that corner. The scale is reasonable for a free surface mode as the wavelength of an *S* wave at 600 Hz is approximately 5 m. Half a wavelength is very close to the size of these drifts. The association is not unambiguous, however, because the data sampling is insufficient to rule out an alternative hypothesis that the ringing is related to inadequate anchoring of that particular sensor. We see this particular ringing on only one sensor. Further, from the geometry of the drift illustrated in Fig. 1 it is not clear why sensor 8 does not show a similar pattern. Finally, it is also noteworthy that comparable ringing is not observed on sensors 19–24 near similar cavities. We conclude resonances are undoubtedly present, but whether the resonance is related to drift geometry, sensor coupling issues, or an influence of large fractures near some sensors is not known. This could be answered by repeating the experiment with a different sensor anchoring method and instrumenting specific wall irregularities with more closely spaced sensors.

A final issue worth noting is that there is evidence for variations in source coupling that further complicate the measurements. Fig. 14 is a common receiver gather from the walkaway experiment recorded by sensor 12. The sources in this profile are at 1 m intervals. The shot timing errors we discussed in Section 3 are evident, but the key point is that throughout the section adjacent shots show wildly different waveforms (e.g. the two waveforms to the left of the gap in the radial record section or the two waveforms to the right of the gap in the transverse record section). This variation cannot be explained by any propagation effect because 1 m is a small fraction of a wavelength (Fig. 12) and standard theory would argue that diffraction should make variations at that scale small. We suggest a more likely explanation is that there is a strong variation in shot coupling to the rock. All the shots used an 'airless jackhammer' that applied a vertical impulse on a pad with a size of approximately 10×10 cm^2. In the walkaway experiment this pad was placed on gravel ballast while in the fan experiment all shots were on a concrete slab the mine poured over most of this area. In both cases the material directly below the shot point is extremely heterogeneous. We know of no published work to model coupling in this kind of medium, but we speculate it would produce a random pattern superimposed on the classic radiation pattern for a vertical force (e.g. Aki & Richards 1980). We suggest the implications of this are much broader than understanding the details of this experiment. Standard source models for earthquakes (e.g. Aki & Richards 1980), nuclear explosions (e.g. Stump 1991), and chemical explosions (e.g. Ziolkowski 1993; Stump *et al.* 1999) assume the source is activated in an approximately homogenous, isotropic medium. These results suggest some of the complexity of real seismic data may be related to near field heterogeneity that makes the standard theoretical models a poor approximation of reality.

7 CONCLUSIONS

We used traveltimes and multiple *P*-wave particle motion methods to show that rocks of the Homestake Formation in the Sanford Underground Research Facility are anisotropic. We find the observations match roughly with predictions from a lattice preferred orientation model computed from similar schist samples from southeastern Vermont with an orientation defined by foliation data collected by Homestake Mine geologists. We attribute the mismatch to the fact that we are using a proxy rock and a homogeneous anisotropic medium approximation. Related modelling

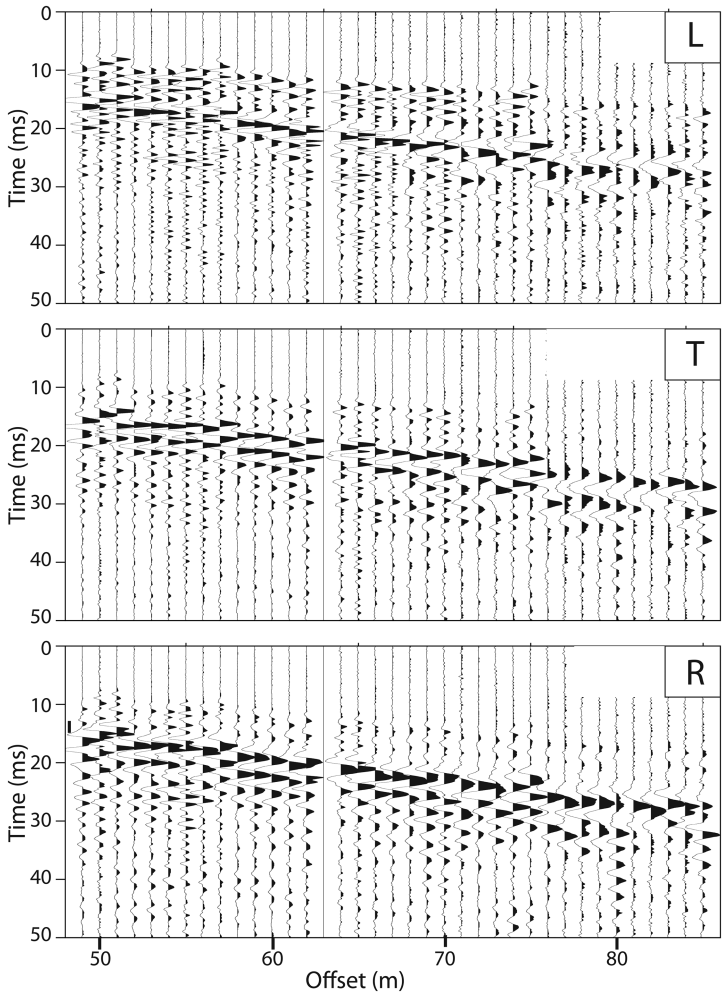

Figure 14. Common receiver gather example. Data shown are from sensor 12 from the walkaway experiment. Components are as defined in Fig. 6. These data have not had statics applied and illustrate uncertainty in shot timing that required us to use statics to estimate velocities accurately. The uncorrected data show negative moveout, which is physically impossible. Component directions are as defined in Fig. 6.

suggests fracture-induced anisotropy can be neglected in the unaltered rock, but may help induce local, large heterogeneity in elastic properties in the damage zone around the mine drifts.

A broader implication of this experiment is that we found the waveforms varied strongly at scales smaller than the range of wavelengths found in the data. We were surprised at the degree of complexity in the waveforms as metamorphic rocks are commonly viewed as transparent to seismic waves. We further show there is clear evidence the data are overprinted with near receiver resonances. Three competing hypotheses are feasible to explain the observed resonance (ringing): sensor coupling, resonances on the free surface defined by the mine drift, and resonances and distortion from fractures in the drift damage zone. We suggest there are at least three other factors that could create scattered waves that further complicate the waveforms: scattering by nearby mine drifts, distortion by fractures near sensors that produce local site effects and scattering by many smaller-scale heterogeneities The first two are oddities of this experiment, but provide important lessons in experiment design in a mine environment. The third is likely found everywhere in the upper crust and are important for high frequency wave propagation in the Earth.

ACKNOWLEDGEMENTS

This paper would not have been possible without the amazing support the staff at SURF provided to collect this experimental data. We especially thank Tom Regan and Neil Engle for keeping us safe underground and being great helpers. Jaret Heise was invaluable in coordinating the experimental work with SURF personnel and getting us access to geologic data from Homestake. Sincere thanks to the DUGL team who fielded the broad-band experiment and to which this experiment was an added component. We also thank Terry Stigall of Indiana University who was a key player in keeping instrumentation working and coming up with her usual creative solutions to problems. Sincere thanks to Jeffrey Park and an anonymous reviewer for constructive comments that helped improve this paper significantly. This paper emerged from the B.S. thesis of JA. The text was extended and revised by all authors led by GLP. The multiwavelet code is the legacy of a body of work by GLP spanning two decades. SJB did the model calculations. The seismic instruments were provided by the Incorporated Research Institutions for Seismology (IRIS) through the PASSCAL Instrument Center at New Mexico Tech. Data used are available through

the IRIS Data Management Center. The facilities of the IRIS Consortium are supported by the National Science Foundation under Cooperative Agreement EAR-1261681 and the DOE National Nuclear Security Administration. This research was supported by the National Science Foundation under EAR-1526894.

REFERENCES

Aki, K. & Richards, P.G., 1980. *Quantitative Seismology: Theory and Methods,* Vol. 1, Freeman, 557p.

Allmendinger, R.W., Cardozo, N. & Fisher, D., 2011. *Structural Geology Algorithms: Vectors and Tensors in Structural Geology,* Cambridge Univ. Press.

Almqvist, B.S.G. & Mainprice, D., 2017. Seismic properties and anisotropy of the continental crust: predictions based on mineral texture and rock microstructure, *Rev. Geophys.,* **55,** 367–433.

Bass, J.D., 1995. Elastic properties of minerals, melts, and glasses, in *Handbook of Physical Constants,* pp. 45–63, ed. Ehrens, T.J., American Geophysical Union.

Bear, L.K. & Pavlis, G.L., 1997. Estimation of slowness vectors and their uncertainties using multi-wavelet seismic array processing, *Bull. seism. Soc. Am.,* **87**(3), 755–769.

Bear, L.K. & Pavlis, G.L., 1999. Multi-channel estimation of time residuals from broadband seismic data using multi-wavelets, *Bull. seism. Soc. Am.,* **89**(3), 681–692.

Bear, L.K., Pavlis, G.L. & Bokelmann, G.H.R., 1999. Multi-wavelet analysis of three component seismic arrays: application to measure effective anisotropy at Piñon Flats, California, *Bull. seism. Soc. Am.,* **89**(3), 693–705.

Beckham, W.E., 1996. Seismic anisotropy and natural fractures from VSP and borehole sonic tools—a field study, *Geophysics,* **61**(2), 456–466.

Brownlee, S.J., Schulte-Pelkum, V., Raju, A., Mahan, K., Condit, C. & Orlandini, O.F., 2017. Characteristics of deep crustal seismic anisotropy from a compilation of rock elasticity tensors and their expression in receiver functions, *Tectonics,* **36,** doi: 10.1002/2017TC004625.

Cardozo, N. & Allmendinger, R.W., 2013. Spherical projections with OSXStereonet, *Comput. Geosci.,* **51,** 193–205.

Cholach, P.Y. & Schmitt, D., 2006, Intrinsic elasticity of a textured transversely isotropic muscovite aggregate: comparisons to the seismic anisotropy of schists and shales, *J. geophys. Res.,* **111,** B09410, doi:10.1029/2005JB004158.

Christensen, N.I., 1965. Compressional wave velocities in metamorphic rocks at pressures to 10 kilobars, *J. geophys. Res.,* **70**(24), 6147–6164.

Christensen, N.I., 1966. Shear wave velocities in metamorphic rocks at pressures to 10 kilobars, *J. geophys. Res.,* **71,** 3549–3556.

Christensen, N.I. & Okaya, D.A., 2007. Compressional and shear wave velocities in South Island, New Zealand rocks and their application to the interpretation of seismological models of the New Zealand crust, *Geophys. Monogr.,* **175,** 123–155.

Crampin, S. & Chastin, S., 2003. A review of shear wave splitting in the crack-critical crust, *Geophys. J. Int.,* **155,** 221–240.

Crampin, S. & Gao, Y., 2013. The new geophysics, *Terra Nova,* **25,** 173–180.

Efron, B., 1979. Bootstrap methods: another look at the jackknife, *Ann. Stat.,* **7,** 1–26.

Erdman, M.E., Hacker, B.R., Zandt, G. & Seward, G., 2013. Seismic anisotropy of the crust: electron-backscatter diffraction measurements from the basin and range, *Geophys. J. Int.,* **195,** 1211–1229.

Fontaine, F.R., Barruol, G., Kennett, B.L.N., Bokelmann, G.H.R. & Reymond, D., 2009. Upper mantle anisotropy beneath Australia and Tahiti from *P* wave polarization: implications for real-time earthquake location, *J. geophys. Res.,* **114,** B03306, doi:10.1029/2008JB005709.

Fouch, M.J. & Rondenay, S., 2006. Seismic anisotropy beneath stable continental interiors, *Phys. Earth planet. Inter.,* **158**(2–4), 292–320.

Hardage, B.A., 1991. *Vertical Seismic Profiling, Part 1: Principles,* Pergamon Press.

Harder, J.O. & Noble, J.A., 1948. Stratigraphy and metamorphism in a part of the northern Black Hills and the Homestake Mine, Lead, South Dakota, *Bull. geol. Soc. Am.,* **59**(9), 941–975.

Hess, H.H., 1964. Seismic anisotropy of the uppermost mantle under oceans, *Nature,* **203,**629–630.

Isaak, D.G., 2001. Elastic properties of minerals and planetary objects, in *Handbook of Elastic Properties of Solids, Liquids, and Gases, Volume III: Elastic Properties of Solid: Biological and Organic Materials, Earth and Marine Sciences,* eds Levy, M. & Stern, R., Academic Press.

Jurkevics, A., 1988. Polarization analysis of three-component array data. *Bull. seism. Soc. Am.,* **78**(5), 1725–1743.

Lefeuvre, F., Turpening, R., Caravana, C., Born, A. & Nicoletis, L., 1993. Vertical open fractures and shear-wave velocities derived from VSPs, full waveform acoustic logs, and televiewer data, *Geophysics,* **58**(6), 818–834.

Leven, J.H., Jackson, I. & Ringwood, A.E., 1981. Upper mantle seismic anisotropy and lithospheric decoupling, *Nature,* **289**(5795), 234–239.

Lilly, J.M. & Park, J., 1995. Multiwavelet spectral and polarization analyses of seismic records, *Geophys. J. Int.,* **122**(3), 1001–1021.

Liu, E. & Crampin, S., 1987. "Effects of Crack-Anisotropy on Cross-Hole Shooting." SEG Abstracts, **57,** 662–64.

Liu, Z., Park, J. & Rye, D.M., 2015. Crustal anisotropy in northeastern Tibetan Plateau inferred from receiver functions: Rock textures caused by metamorphic fluids and lower-crust flow?, *Tectonophysics,* **661,** 66–80,

Mainprice, D, Heilsche, R. & Schaeben, H., 2015. Calculating anisotropic physical properties from texture data using the MTEX open-source package, in *Deformation Mechanisms, Rheology and Tectonics: Microstructures, Mechanics and Anisotropy,* Vol. 360, pp. 175–192, eds Prior, D.J., Rutter, E.H. & Tatham, D.J., Geological Society London Special Publications.

Mandic, V., Tsai, V.C., Pavlis, G.L., Prestegard, T., Bowden, D.C., Meyers, P. & Caton, R., 2018. A 3D broadband seismometer array experiment at the homestake mine, *Seismol. Res. Lett.,* **89**(6), 2420–2429.

Mark, H.F., Lizarralde, D., Collins, J.A., Miller, N.C., Hirth, G., Gaherty, J.B. & Evans, R.L., 2019. Azimuthal seismic anisotropy of 70-Ma Pacific-plate upper mantle. *J. geophys. Res.,* **124,** 1889–1909.

Noble, J.A., Harder, J.O. & Slaughter, A.L., 1949. Structure of a part of the northern Black Hills and the Homestake Mine, Lead, South Dakota, *Bull. geol. Soc. Am.,* **60**(2), 321–352.

Okaya, D.A., Vel, S.S., Song, W.J. & Johnson, S.E., 2019. Modifications of crustal seismic anisotropy by geologic structures ["structural geometric anisotropy"], *Geosphere,* **15**(1), 146–170.

Oliver, J.E., Cook, F.A. & Brown, L., 1983. COCORP and the Continental Crust, *J. geophys. Res.,* **88**(B4), 3329–3347.

Park, J. & Levin, V., 2016. Anisotropic shear zones revealed by back-azimuthal harmonics of teleseismic receiver functions, *Geophys. J. Int.,* **207,** 1216–1243.

Petersson, N.A. & Sjögreen, B., 2015. Wave propagation in anisotropic elastic materials and curvilinear coordinates using a summation-by-parts finite difference method, *J. Comput. Phys.,* **299,** 820–841,

Petersson, N.A. & Sjögreen, B., 2017a. SW4 User's Guide, v. 2, Computational Infrastructure for Geodynamics, Davis, CA, doi:10.5281/zenodo.1045297.

Petersson, N.A. & Sjögreen, B., 2017b. User's guide to SW4, version 2.0, Technical report LLNL-SM-741439, Lawrence Livermore National Laboratory, Livermore, CA.

Reading, A., Kennett, B. & Sambridge, M., 2003. Improved inversion for seismic structure using transformed, *S*-wavevector receiver functions: Removing the effect of the free surface, *Geophys. Res. Lett.,* **30**(19), 1981, doi:10.1029/2003GL018090.

Roggenthen, W.M. & Berry, K.M., 2016. Acoustic velocities and pillar monitoring of the 4850 level of the Sanford Underground Research Facility, in *Proceeding of 50th US Rock Mechanics/Geomechanics Symposium,* ARMA 16–0411.

Roggenthen, W.M. & Koch, C.D., 2013. Geophysical logging of DUSEL core and geotechnical application, *Proceeding of 47th US Rock Mechanics/Geomechanics Symposium,* ARMA 13–493.

Romanowicz, B. & Wenk, H., 2017. Anisotropy in the deep Earth, *Phys. Earth planet. Inter.,* **269,** 58–90.

Schulte-Pelkum, V. & Mahan, K.H., 2014. A method for mapping crustal deformation and anisotropy with receiver functions and first results from USArray, *Earth planet. Sci. Lett.,* **402,** 221–233.

Shearer, P.M. & Orcutt, J.A., 1986. Compressional and shear wave anisotropy in the oceanic lithosphere—the Negendei seismic refraction experiment, *Geophys. J. R. astr. Soc.,* **87,** 967–1003.

Silver, P.G. & Chan, W.W., 1991. Shear wave splitting and subcontinental mantle deformation. *J. geophys. Res.,* **96**(B10), 16 429–16 454.

Strang, G. & Nguyen, T., 1996. *Wavelets and Filter Banks,* Wellesley-Cambridge Press, 490p.

Stump, B.W., 1991. Nuclear explosion seismology: verification, source theory, wave propagation and politics, *Rev. Geophys.,* **29,** 734–741.

Stump, B.W., Pearson, D.C. & Reinke, R.E., 1999. Source comparisons between nuclear and chemical explosions detonated at Rainier Mesa, Nevada Test Site, *Bull. seism. Soc. Am.,* **89**(2), 409–422.

Svenningsen, L. & Jacobsen, B.H., 2004. Comment on "Improved inversion for seismic structure using transformed, *S*-wavevector receiver functions: Removing the effect of the free surface" by Any Reading, Brian Kennett, & Malcom Sambridge, *Geophys. Res. Lett.,* **31,** L24609, doi:10.1029/2004GL021413.

Thomson, D., 1982. Spectrum estimation and harmonic analysis, *Proc. IEEE,* **70,** 1055–1096.

Tsvankin, I., Gaiser, J., Grechka, V., van der Baan, M. & Thomsen, L., 2010. Seismic anisotropy in exploration and reservoir characterization: an overview, *Geophysics,* **75**(5), doi:10.1190/1.3481775.

VanderBeek, B.P. & Toomey , D.R., 2017. Shallow Mantle Anisotropy beneath the Juan de Fuca Plate, *Geophys. Res. Lett.,* **44**(22), 382, doi:10.1002/2017GL074769.

Walker, A.M. & Wookey, J., 2012. MSAT—a new toolkit for the analysis of elastic and seismic anisotropy, *Comput. Geosci.,* **49,** 81–90.

Wenk, H-R., Kanitpanyacharoen, W. & Voltolini, M., 2010, Preferred orientation of phyllosilicates: comparison of fault gouge, shale and schist, *J. Struct. Geol.,* **32,** 478–489.

Ziolkowski, A., 1993. Determination of the signature of a dynamite source using source scaling, Part 1: theory, *Geophysics,* **58**(8), 1174–1182.

SUPPORTING INFORMATION

Supplementary data are available at *GJI* online.

Figure S1. 3DPDF illustrating the geometry of Homestake Mine site. The figure has 13 elements that can be turned on and off through the Model Tree menu: seven elements that illustrate mine drifts and shafts; 'Topography' shows surface topography as a translucent surface; two elements ('North Arrow' and 'North Label') are used to provide a geographic reference; 'Broad-band Station Locations' are spheres drawn at the location of broad-band seismic stations described by Mandic *et al.* (2018); locations of the HSP experiments that are the topic of this paper are illustrated as gold coloured rectangles; and 'Surface Weight Drop Locations' are small yellow spheres drawn at the location of all weight drop sources recorded by the broad-band array (not used in the paper). At the current time this figure is best viewed by Acrobat Reader. To understand the geometry requires interaction with the figure zooming, panning, and turning features on an off.

Figure S2. Photograph showing use of alignment jig to orient geophones. The left edge of the jig here is aligned with the man car rail that provides a straight line reference for direction. The parallelogram transfers this direction to the sensor long axis as illustrated. A typical plaster base is seen for this sensor that was set on a concrete slab.

Figure S3. Example of visualization of particle motion time-series data produced by multiwavelet method. Parts (a), (b) and (c) are the longitudinal (L), radial (R) and transverse (T) components (respectively) of the seismogram that was analysed to produce the lower three panels. The seismograms were produced by filtering the raw data with a five-pole Butterworth filter in the same band as the mulitwavelet set used in the analysis (200–600 Hz) and plotting at a constant gain. (d) plots the estimated azimuthal angle and (e) the zonal angle defined as illustrated in Fig. 6. (f) plots amplitude as a function of time in decibels. The translucent grey box outlines the section of the data averaged by multiwavelets that define the estimates at the position of the centre line through the box. In terms of the theory m_0 in eq. (S.5) for this example is $N/2$.

Figure S4. Illustration of time averaging of particle motion estimates. (a) shows longitudinal seismograms from one sensor (sensor 10 of field file id 225). In this portion and later portions the full signal is shown as a dashed line and the signal with a tail mute is shown as a solid line. The two signals are offset and aligned so 0 lag defines the right side of the analysis wavelets for clarity. This is the alternate choice for $m_0 = 0$ in eq. (S.6) versus $N/2$ illustrated in Figure S3. (b) shows major axis angle deviations from longitudinal ($\delta\theta$ angle defined in eq. S.28) computed with the full signal (dashed curve) and data with a tail mute to remove *S* phase. (c) Illustrates amplitude of the estimated major axis as a function of time in dB relative to the largest amplitude in the time window illustrated. The translucent blue rectangle shows the maximum range the algorithm would consider for particle motion averaging. The smaller, translucent, grey box is the maximum window size for the time average. The red lines in (b) illustrate the signal-to-noise threshold used to position the start time of the averaging window. The orange line in (b) illustrates the final angle estimate computed as the median of the estimates inside the grey box.

Please note: Oxford University Press is not responsible for the content or functionality of any supporting materials supplied by the authors. Any queries (other than missing material) should be directed to the corresponding author for the paper.